Boundary conditions for a two-dimensional direct kinetic simulation of a Hall thruster

IEPC-2019-613

Presented at the 36th International Electric Propulsion Conference
University of Vienna, Austria
September 15-20, 2019

Astrid L. Raisanen*
University of Michigan, Ann Arbor, MI 48109, USA

Iain D. Boyd†
University of Colorado, Boulder, CO 80309, USA

A direct kinetic (DK) simulation is capable of modeling the non-equilibrium state of a plasma without the numerical noise that is inherent to particle-based methods, since the velocity distribution functions (VDFs) are obtained in a deterministic manner. In this work, a quasi-one-dimensional fluid electron algorithm is used in conjunction with a two-dimensional DK method for neutral atoms and ions, to model the discharge plasma in a Hall thruster channel and near-field plume. Diffuse wall boundary conditions ensure particle conservation and result in satisfactory agreement between results for the hybrid-DK model and a comparable hybrid-particle-in-cell (PIC) model. Additionally, the DK inlet boundary condition is examined, and convergence is found for reasonable resolution of the neutral distribution downstream of the inlet location. Improvements are made to the electron model, i.e. the current solver is modified to ensure that the anode sheath potential is taken into account, and preliminary updates are performed so that the hybrid-DK model is better equipped to resolve more complex physical processes inside the thruster channel.

Nomenclature

f	= distribution function
$\vec{E}$	= electric field, T
m	= mass, kg
F	= flux of VDF
c	= CFL number
v	= velocity, m/s
z, r	= axial and radial components
a	= acceleration
r_k	= slope factor
Ψ	= nonlinear limiter function
j_e	= electron current density, A/m
p_e	= electron pressure, Pas
n	= number density, m^{-3}
e	= elementary charge, 1.602×10^{-19}C
I_T	= total current, A
ϕ^*	= thermalized potential, V
$\vec{B}$	= magnetic field, T
T_e	= electron temperature, eV
λ	= magnetic field streamline
ν	= collision frequency, s^{-1}
ϕ	= potential, V
μ_e	= electron mobility, $m^2V^{-1}s^{-1}$
Γ	= particle flux, m^{-3}
A	= cross sectional area, m^2
σ	= electrical conductivity, Ω·m

*Ph. D. Candidate, Aerospace Engineering, astridr@umich.edu.
†H.T. Sears Memorial Professor, Aerospace Engineering Sciences, iain.boyd@colorado.edu.

I. Introduction

The Hall effect thruster (HET), a space propulsion device often used for applications including satellite station keeping and orbit raising, is an electrostatic accelerator. It utilizes the Hall effect to confine electrons and a large electric field to accelerate ions and generate thrust. HETs were first used on board satellites in the early 1970s in the former Soviet Union.[1] Modeling efforts for these devices have been ongoing, and some more recent work has focused on the azimuthal, cross-field electron drift instability.[2] However, to calculate macroscopic quantities of interest including thrust and specific impulse (Isp), an axial-radial (z, r) simulation is required. A hybrid particle-in-cell (PIC) method is a relatively common modeling approach, wherein electrons are treated as a fluid, and more massive neutral atoms and ions are modeled as particles. Fife, Hagelaar *et. al*, and Koo and Boyd developed two-dimensional (z, r) hybrid-PIC simulations in the late 1990s and early 2000s.[3–5] While PIC techniques are robust, they are inherently susceptible to numerical noise.[6] Such noise can distort the frequency output of the plasma response and may not allow for proper resolution of the non-equilibrium velocity distribution functions (VDFs) of the ions.

In this work, a direct kinetic (DK) algorithm is used to model neutral atoms and ions in an axial-radial configuration. The deterministic DK method does not contain stochastic noise, and it has been assessed in previous studies for both one-dimensional and two-dimensional HET discharge plasmas.[7,8] In the present study, the goal is to ensure that boundary conditions for the DK scheme are implemented correctly so that results correspond well with comparable PIC simulation results. Additionally, we examine DK grid discretization, particularly in the presence of an incoming jet of neutral particles. Lastly, the electron algorithm and its boundary conditions are examined with the intention of making the model more robust to handle complex two-dimensional plasma simulations. The paper is set up as follows: in Section II, we review the general numerical method for the DK and electron algorithms; in Section III, we elaborate on boundary condition updates; and in Section IV, we present results that implement those updates.

II. Hybrid-DK Numerical Method

A. Modeling neutral atoms and ions

The DK model uses a second-order accurate, finite volume solution technique with a modified Arora-Roe limiter to calculate the numerical flux of kinetic quantities through each cell interface.[9] Strictly speaking, the simulation domain is planar, since the numerical method contains two dimensions in physical and velocity space for both ions and neutral atoms. Although not shown here, we verify that the differences between the planar (2D2V) and axisymmetric (2D3V) algorithms for neutral atoms are insignificant for the present work. This finding agrees with the literature, so we use the conventional notation to describe an axial-radial (z, r) domain.[3]

For singly charged ions and neutral atoms, the distribution function, f, evolves over time, t; physical space, z and r; and velocity space, v_z and v_r, according to the following kinetic equations:

$$\frac{\partial f_i}{\partial t} + v_z \frac{\partial f_i}{\partial z} + v_r \frac{\partial f_i}{\partial r} + \frac{eE_z}{m_i} \frac{\partial f_i}{\partial z} + \frac{eE_r}{m_i} \frac{\partial f_i}{\partial r} = S_i, \tag{1}$$

$$\frac{\partial f_n}{\partial t} + v_z \frac{\partial f_n}{\partial z} + v_r \frac{\partial f_n}{\partial r} = S_n. \tag{2}$$

In Eq. (1), ions accelerate due to the force from the electric field, $\vec{E} = (E_z, E_r)$. The general collision term is denoted by S, and it is calculated as the sum of collisions due to singly charged ionization, which is discussed in Section II C.

To achieve numerical stability, the Courant Friedrichs Lewy (CFL) condition must be met, i.e. the total CFL number should always be less than 1:

$$\sum_i \left(\frac{\max |v|_i \Delta t}{\Delta z_i} + \frac{\max |a|_i \Delta t}{\Delta v_i} \right) \leq 1, \tag{3}$$

where i denotes the dimension.

1. Flux calculation

The discretized equation for advection in axial, physical space can be written as a function of the flux, F, which passes through the k-th cell's interfaces, located at *k-1/2* and *k+1/2*,

$$f_k^{q+1} = f_k^q - (F_{k+1/2} - F_{k-1/2}), \tag{4}$$

where $F = \frac{v_z \Delta t}{\Delta z} f = cf$, and c represents the CFL number in physical space. Superscript q and subscript k denote the time step and physical cell, respectively, and $f = f_{iz,ir,jz,jr}$ is the discretized VDF in the k-th cell. The subscripts i and j denote the specific location of the VDF in physical space and velocity space, respectively.

According to the monotonic upwind scheme for conservation laws (MUSCL), the flux due to positive axial advection through the interface *k-1/2* can be described as:

$$F_{k-1/2}^{+} = cf_{k-1} + \frac{(1-|c|)c}{2}(f_k - f_{k-1})\Psi r_{k-1/2}, \tag{5}$$

where $r_{k-1/2}$ is the slope factor, which indicates the smoothness of the neighboring values. For this positive advection case, $r_{k-1/2}$ is dependent on the VDF in the k-th cell and the two adjacent cells upstream:

$$r_{k-1/2} = \frac{f_{k-1} - f_{k-2}}{f_k - f_{k-1}}. \tag{6}$$

The corresponding value of the Arora-Roe limiter, Ψ, can be described by:[10]

$$\Psi = \frac{1+|c|}{3}(r-1) + 1. \tag{7}$$

The slope factor is used to achieve monotonicity. For example, if r for the positive advection case is also positive, the second term on the right hand side of Eq. (5) contributes to the positive evolution of f. Otherwise, it acts as an anti-diffusive flux term to limit numerical oscillations. For the DK simulation, there are three bounds for the limiter that are discussed in Ref. 9.

2. Kinetic boundary conditions

Four types of boundary conditions are implemented at the edges of the simulation domain, which is shown in Fig. 1a. These include: an outflow condition for ions leaving the domain; outflow with allowance for inflow of neutral particles if there is a nonzero background pressure; a specular reflection (zero flux) boundary condition at the thruster centerline; and wall boundaries at which neutral atoms are diffusely reflected, and ions recombine to atoms and reflect diffusely. The wall boundary is discussed in detail in Section III A.

Two ghost cells adjacent to each boundary cell are available for information exchange. At simulation boundaries, zeroth order extrapolation of the VDF is used, implying that updates at the boundaries are of first order accuracy. Since the same information is extrapolated to both of the ghost cells adjacent to any boundary, this means that the slope factor, r, is zero, and the flux through the boundary cell is dependent only on the VDF in the cell directly adjacent to the boundary. This is important, as it allows one to ensure strict particle conservation at simulation boundaries. For example, for the positive, axial ion outflow condition, shown in Fig. 1b, the VDFs in positive, axial velocity space are extrapolated to adjacent ghost cells, and the VDFs for negative, axial velocity space in the ghost cells are set to zero. Therefore, ions exit across the boundary, and no ions may re-enter the domain. At the thruster centerline ($r = 0$), a zero net flux condition is applied, and particles that cross the centerline are specularly reflected back into the domain. This is accomplished by first extrapolating the VDF for $v_r < 0$ to the adjacent ghost cells and then performing a coordinate transform on the same portion of the VDF, mirroring it in positive velocity space.

B. Modeling electrons

Electrons are considered to be at a steady state on the time scale of ions. Along a magnetic field streamline, thermal equilibrium of confined electrons is assumed, allowing for the approximation of constant electron temperature. Assuming an isotropic Maxwellian distribution for electrons, we apply a quasi-one-dimensional fluid electron algorithm, similar to the approach used by Koo and Boyd, Fife, and Hagelaar *et al.*[3–5]

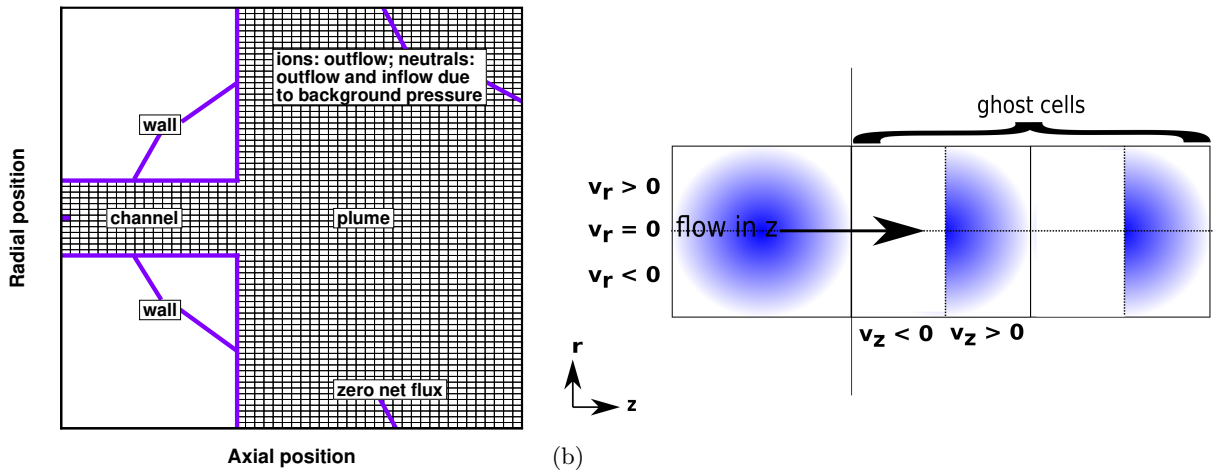

(a) (b)

Figure 1. In (a), the DK simulation grid is shown, and in (b), the outflow boundary condition for ions is highlighted.

1. *Electron Momentum and Current Conservation*

Across lines of force, i.e. perpendicular to the magnetic field streamlines, the force balance on electrons is described by the one-dimensional Ohm's Law, also known as the drift-diffusion approximation.[11] Time dependence and inertial effects are neglected in this approximation:

$$j_{e,\perp} = \sigma \left(E_\perp + \frac{\nabla_\perp p_e}{n_e e} \right), \tag{8}$$

where $j_{e,\perp}$ is the electron current density perpendicular to the magnetic field, and $E_\perp$ is the perpendicular electric field. Note that the electron grid is comprised of a discrete number of magnetic field streamlines. The λ grid used in the benchmarking portion of this study in Section IV B is shown in Fig. 2.

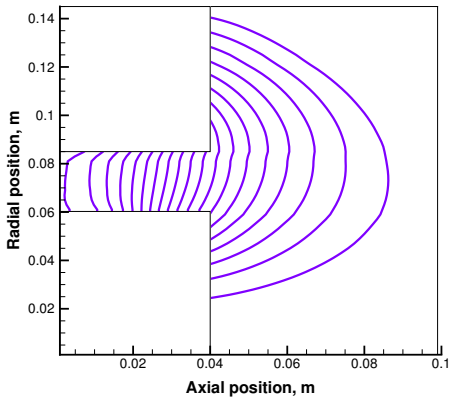

Figure 2. The UM/AFRL P5 electron λ grid used in this study.

Assuming there is no charge buildup in the device, the total current, which includes the sum of the ion and electron contributions, is conserved. The expression for the total current, I_T, can be given as:

$$I_T = \sum_{\lambda_a}^{\lambda_c} \int_S e n_i v_i \partial S + \frac{\phi^*(\lambda_a) - \phi^*(\lambda_c)}{d\lambda} \sum_{\lambda_a}^{\lambda_c} \int_S e n_e \mu r B \partial S - \sum_{\lambda_a}^{\lambda_c} \int_S e n_e \mu r B [\ln\left(\frac{n_e}{n_e^*}\right) - 1] \frac{k_b}{e} \frac{\partial T_e}{\partial \lambda} \partial S, \tag{9}$$

where n_e^* is a reference plasma density, set to a constant value of 10^{12} m^{-3} for this work. S represents a λ surface, and summation occurs between the virtual anode, λ_a, and the virtual cathode, λ_c. In order to calculate the total current, the thermalized potential at the anode and cathode λ-lines must be known. In this model, ϕ^* is assumed to float at these locations, but ϕ is fixed. An alternate method for the current calculation that allows for variation in the anode potential due to a sheath potential drop is considered in Section III D.

From the total current, the thermalized potential, ϕ^*, can be calculated via a simplified expression of Eq. (8), namely:

$$j_{e,\perp} = en_e\mu rB\left(-\frac{\partial\phi^*}{\partial\lambda} - \left[\ln\left(\frac{n_e}{n_e^*}\right) - 1\right]\frac{k_b}{e}\frac{\partial T_e}{\partial\lambda}\right). \tag{10}$$

The thermalized potential is a reduced description of the plasma potential, and it is the result of the integration of electron momentum along a magnetic field streamline. If ϕ^* is known, the two-dimensional plasma potential, $\phi(\lambda, r)$, can be calculated via the expression for ϕ^*:

$$\phi(\lambda, r) = \phi^*(\lambda) + \frac{k_b T_e(\lambda)}{e}\ln\left(\frac{n_e(\lambda, r)}{n_e^*}\right). \tag{11}$$

The electric field ($\vec{E} = -\nabla\phi$) is obtained from the potential distribution.

2. Electron Energy Conservation

Information regarding the numerical implementation of the electron energy conservation equation can be found in Ref. 12, but we include a brief description in order to describe the energy loss and electron mobility terms. Assuming a Maxwellian distribution, electron mean energy, $\epsilon = \frac{3}{2}\frac{k_b T_e}{e}$, is transported via advection and diffusion, which are balanced by Ohmic heating and elastic and inelastic energy losses. The general form of the equation is as follows:

$$\frac{\partial(n_e\epsilon)}{\partial t} + \nabla\cdot(n_e\epsilon\vec{u}_e + p_e\vec{u}_e + \vec{q_e}) = \vec{j}_e\cdot\vec{E} - \Lambda_i, \tag{12}$$

where $\vec{q}_e$ represents heat conduction, and Λ_i represents the energy loss term, which consists of inelastic collisions and wall heat losses. Note that elastic losses are considered to be negligible.

In the present study, we consider electron energy losses associated with excitation and ionization from the ground state as well as electron-wall losses, based on the computational models of Boeuf and Garrigues.[13] Λ_i is described by:

$$\Lambda_i = n_e\epsilon\nu(\epsilon), \tag{13}$$

where $\nu(\epsilon)$ represents the frequency of electron energy losses. The frequency of electron energy loss due to excitation and ionization from the ground state is described by:

$$\nu(\epsilon)_{e-Xe} = n_n k_{e-Xe}(\epsilon), \tag{14}$$

where $k_{e-Xe}(\epsilon)$ represents the loss rate due to singly charged ionization from the ground state. The frequency of electron energy loss to the walls is described by:

$$\nu(\epsilon)_{walls} = 10^7\alpha_w\exp\left(\frac{-U_{loss}}{\epsilon}\right), \tag{15}$$

where U_{loss} represents the potential barrier due to the formation of a dielectric sheath at the walls and is set to 20 eV, and $\alpha_w < 1$ represents the relative frequency of electron-wall collisions.

The electron mobility ($\mu = \frac{\sigma}{en_e}$) perpendicular to the magnetic field is a function of the electron momentum transfer frequency, ν_m, and the Hall parameter, Ω:

$$\mu_{e,\perp} = \frac{e}{m_e\nu_m}\frac{1}{1+\Omega^2}, \tag{16}$$

where $\Omega = \frac{\omega_{B,e}}{\nu_m}$, and $\omega_{B,e}$ is the electron cyclotron frequency. In this study, ν_m is augmented to account for effects of non-classical electron transport. The electron-neutral collision frequency, electron-wall collision

frequency, and effective Bohm collision frequency are calculated via the following expressions:

$$\nu_{neut} = 2.5 \times 10^{-13} n_n, \tag{17}$$

$$\nu_{e,wall} = 10^7 \alpha_w, \tag{18}$$

$$\nu_{Bohm} = \alpha_b \omega_{B,e}. \tag{19}$$

Note that α_w in Eq. (18) is also used in Eq. (15) to calculate electron energy losses via electron-wall collisions.

C. Ionization Collisions

Since the significantly more massive neutral particles move much more slowly than the electrons, the ionization rate, $\dot{n}_{ion}$, can be approximated as a function of the mean electron energy, ϵ:[14]

$$\dot{n}_{ion} = n_n n_e \zeta(\epsilon), \tag{20}$$

where the electron density, n_e, is equal to the ion density, n_i, due to the quasineutral assumption. To account for DK ionization collisions, the ionization rate is multiplied by the normalized distribution function in each Cartesian cell at each time step:

$$S_i(\vec{v}, \vec{z}, t) = \beta \dot{n}_{ion} \hat{f}_n(\vec{v}), \tag{21}$$

where β is $+1$ or -1, depending on whether an ion is created or a neutral atom is deleted. For each ionization event, a neutral atom is deleted, and an ion with the identical velocity and physical location is created, conserving the total number of particles in the system. Velocity mapping is discussed in Ref. 9.

III. Numerical model updates

A. Modeling wall collisions

At wall boundaries, ions recombine to neutral atoms and reflect diffusely, and neutral atoms simply reflect diffusely. Since spatial resolution is only as small as a physical Cartesian cell, the particle flux must be calculated accurately at boundaries. Expressions in this section refer to the conservation of number density, but in reality, the number of particles in the simulation domain are conserved, since the calculations are performed in each physical cell. For derivations in this section, we consider only particle reflections at the outer channel wall.

1. Neutral particle reflections

For neutral particles, the outgoing VDF is extrapolated to the neighboring ghost cells so that particles are advected out of the simulation domain, i.e. they collide with the wall, according to the first term in Eq. (5). The number of particles that flux through the interface over a single time step is:

$$\Gamma_{n,out} = \frac{\int_t \int_0^{v_{r,max}} \int_{v_{z,min}}^{v_{z,max}} v_r \cdot f_{n,out}(v_z, v_r) dv_z dv_r dt}{\int dr}, \tag{22}$$

where $v_{z,min}$ and $v_{z,max}$ represent the limits of velocity space in the z-direction, $v_{r,max}$ represents the upper limit of velocity space in the r-direction, and $f_{n,out}$ is the non-normalized VDF in the cell inside the domain, adjacent to the boundary. Since particles are advected in the positive r direction, toward the outer wall of the thruster, only positive velocity space ($v_r > 0$) is considered.

The number of particles that flux out of the system is equal to the number of particles that re-enter the domain, i.e. $\Gamma_{n,in} = \Gamma_{n,out}$. The incoming particle flux is described by:

$$\Gamma_{n,in} = \frac{\int_t \int_{v_{r,min}}^{0} \int_{v_{z,min}}^{v_{z,max}} |v_r| \cdot f_{n,in}(v_z, v_r) dv_z dv_r dt}{\int dr}, \tag{23}$$

where $f_{n,in}$ is:

$$f_{n,in}(v_z, v_r) = n_n \hat{f}_{n,in}(v_z, v_r), \tag{24}$$

and $\hat{f}_{n,in}$ is the normalized, reflected VDF. At the outer channel wall, the reflected VDF ($v_r < 0$) into the domain is described by a half Maxwellian distribution at the wall temperature, assuming a perfectly diffuse reflection. The Maxwellian VDF in two dimensions can be written as:

$$f_{Maxwell}(v_z, v_r) = \left(\frac{m}{2\pi k_b T_w}\right) \exp\left(-\frac{m}{2k_b T_w}(v_z^2 + v_r^2)\right), \tag{25}$$

where T_w is the wall temperature. This is normalized as:

$$\hat{f}_{n,in}(v_z, v_r) = \frac{f_{Maxwell}(v_z, v_r)}{\int_{v_{r,min}}^{0} \int_{v_{z,min}}^{v_{z,max}} f_{Maxwell}(v_z, v_r) dv_z dv_r}. \tag{26}$$

Since $\hat{f}_{n,in}$ is known, we simply insert Eq. (24) into Eq. (23) and solve for n_n by setting equal the number of particles that flux out of and into the system.

2. Ion particle reflections

The ion advection algorithm is conducted over a single time step, and the appropriate information is stored and transferred to the neutral subroutine so that recombined neutrals can be introduced into the simulation domain in the same manner as reflected neutrals. The number of particles advected out of the domain, subject to the ion CFL condition, must be equal to the number of particles that return, subject to neutral advection, and considering the fact that advection in time conforms to a second-order Runge-Kutta method.[9] This means that there are two steps for integration, and advection in r occurs twice over a single time step. The count of fluxed ions, $\Gamma_{i,out}$, is calculated via the expression in Eq. (22), using the parameters for ion velocity space. It is summed over two integration steps and stored. The recombined density introduced to the domain over a full time step then conforms to:

$$n_{n,re} = \frac{\Gamma_{i,out}}{\int_t \int_{v_{r,min}}^{0} \int_{v_{z,min}}^{v_{z,max}} |v_r| \cdot \hat{f}(v_z, v_r) dv_z dv_r dt / \int dr}, \tag{27}$$

so that $\Gamma_{i,out} = \Gamma_{n,re}$.

The VDF for all reflected particles is described by:

$$f_{n,in}(v_z, v_r) = (n_n + n_{n,re})\hat{f}_{n,in}. \tag{28}$$

B. Neutral injection technique

In the present work, the input parameters for neutral injection at the anode are the mass flow rate, $\dot{m}$, and the radial location of the anode injector, located at an axial position of $z = 0$. The anode injector should include an integer number of computational cells. A neutral density is assigned to the ghost cells adjacent to the inlet assuming that particles are injected at a thermal velocity corresponding to the anode inlet temperature, i.e.

$$n_{inlet} = \frac{\dot{m}}{m_i < v_z > A}, \tag{29}$$

where $A = \pi(r_2^2 - r_1^2)$ is the cross sectional area of the slit through which the particles enter, and $< v_z >$ is the average velocity of a half Maxwellian distribution biased with axial velocity at the anode temperature. Strictly speaking, the inlet area should correspond to the two-dimensional DK domain, but we elect to use the same inlet area as is used in the axisymmetric PIC simulation so that the injection techniques are the same.

$$< v_z >= \int_{v_{r,min}}^{v_{r,max}} \int_{0}^{v_{z,max}} v_z \left(\frac{m_i}{2\pi k_b T_a}\right) \exp\left(-\frac{m_i}{2k_b T_a}(v_z^2 + v_r^2)\right) dv_z dv_r, \tag{30}$$

where T_a is the anode reservoir temperature. The analytical values for the integrals in Eq. (30) are calculated using $I_1(a) = \frac{1}{2a}$ and $I_0(a) = \frac{1}{2}\left(\frac{\pi}{a}\right)^{\frac{1}{2}}$ where $I_n(a) = \int_0^\infty x^n \exp(-ax^2)dx$, and the expression simplifies to:[15]

$$< v_z >= \sqrt{\frac{k_b T_a}{2\pi m_i}}. \tag{31}$$

Thus, the flux of particles through the anode orifice into the simulation domain is:

$$\Gamma_{n,inlet} = \frac{n_{inlet} \int_t \int_{v_{r,min}}^{v_{r,max}} \int_0^{v_{z,max}} v_z \cdot f_{Maxwell}(v_z, v_r) dv_z dv_r dt}{\int dz}. \tag{32}$$

The resultant particle flux correlates exactly with the standard particle flux calculation for free molecular flow with no stream velocity onto a surface, i.e. $\Gamma = \frac{n}{4}\sqrt{\frac{8k_bT}{\pi m}}$ per unit area, per unit time.[16]

C. Electron algorithm boundary conditions

The near-anode region of a HET typically displays a relatively low electron temperature (3-6 eV), a small applied magnetic field, little or no electric field, and relatively high diffusion of electrons. Neutral particles from the anode injector move downstream toward the ionization region, and back-streaming ions travel toward the anode.[17] However, the quasi-one-dimensional electron model does not correctly recover the diffusion region. The model actively solves the electron fluid equations starting at the virtual anode location, which is slightly offset from the anode face in Fig. 2, and information upstream of the virtual anode is extrapolated.

Near the anode, the current contribution from electrons should be high compared to that from ions, since positively-moving ions are slow, and back-streaming ions contribute negatively to the total current. From Eqn. (10), if the electron temperature and the potential are nearly constant in the near-anode region, the calculated electron current density is small, implying that the non-zero contribution from electron pressure in this region may not be accurately calculated. The electron current density can be increased in the near-anode region via a large cross-field electron mobility term, but to reduce variability of input parameters in the benchmarking portion of this study, we do not consider multi-region Bohm transport models and instead elect to use simulation boundary conditions that provide solution stability.

In comparable PIC simulations, it is common to apply Dirichlet boundary conditions for both the potential and electron temperature at the virtual anode and cathode locations.[4,5] Often, threshold limits are applied to the plasma potential to ensure that it will not fluctuate beyond the values that are applied at the anode and cathode. In this work, we find that the hybrid-DK simulation is sensitive to the applied boundary conditions and threshold limits, particularly if they are too restrictive, since the plasma properties are well resolved. If the plasma is constrained due to artificial plasma limiters, it will evolve to a non-physical solution.

D. Current conservation

The current calculation method discussed in Section II 1 (Eq. (9)) assumes that the potential is fixed at the virtual anode and cathode locations. Strictly speaking, the anode potential is not fixed, since a potential drop is often present due to the formation of a plasma sheath. To take into account an electron-repelling anode sheath in the calculation of the discharge current, we implement a solution technique similar to that used by Parra *et. al.*[18].

The ground potential is assigned at the virtual cathode (usually $V_c = 0$), and an initial guess is assigned for the discharge current, I_d, based on the value at the previous time step. Then, using the assigned discharge current and a newly updated value for $T_e(\lambda)$, $\frac{\partial \phi^*}{\partial \lambda}$ (Eq. (10)) is calculated everywhere upstream of the cathode, taking into account the potential fall due to a plasma sheath at the virtual anode.

Using classical electrode theory in the limit of a collisionless, thin sheath and assuming that the ion Bohm condition is met at the sheath edge, the sheath potential drop at the anode can be written as:

$$\phi_a = \frac{-k_bT_e}{e} \ln \left[\left(\frac{I_T}{Aen_e\sqrt{\frac{k_bT_e}{2\pi m_e}}} \right) + \exp\left(-\frac{1}{2}\right)\sqrt{\frac{2\pi m_e}{m_i}} \right], \tag{33}$$

where A is the anode area, and ϕ_a is the potential drop at the anode.

Using $\phi(\lambda_a) = V_d + \phi_a$, a Newton-Raphson solver produces a new guess for I_d, and the process is repeated until the potential at the anode is satisfactory within a tolerance of approximately 0.5 V. Typically, 3-4 iterations are required for convergence.

IV. Results demonstrating model improvements

A. Neutral injection and grid convergence

Previous benchmarking results indicated that comparable DK and PIC simulation injection techniques did not entirely agree.[7] Using the injection technique discussed in Section III A, we achieve agreement between the DK and PIC injection methods, and the results for a full plasma simulation in Section IV B corroborate this assertion. In this section, we focus on the effects of physical and velocity grid discretization in the presence of an incoming jet of neutral particles.

It is known that DK methods resolve thermal distributions well but are not ideally suited for beam-type distributions that fixed velocity bins cannot resolve.[19] In this section, we demonstrate that, if an inlet is small compared to the domain size, the resolution of both physical and velocity space with respect to the inlet size are important. We consider cases in which neutral atoms are injected from the left hand side of the domain through an inlet with a height of 2 mm. The inlet is comprised of one, two, or three cells with coarse or fine velocity grid discretization. The cases are referred to Cases 1, 2, and 3, respectively, with a denoting coarse velocity bins and b denoting fine velocity bins. The case details and their associated computational times are shown in Table 1. Note that the time step, Δt, changes with cell size so that the CFL number is the same for each simulation.

Table 1. Neutral injection simulation parameters

	Δt	$\Delta z, \Delta r$	$\Delta v_z, \Delta v_r$	Wall time
Case 1a	1×10^{-6} s	(2, 2) mm	(25, 10) m/s	0.3 hr/ms
Case 1b	1×10^{-6} s	(2, 2) mm	(10, 4) m/s	2.0 hr/ms
Case 2a	5×10^{-7} s	(1, 1) mm	(25, 10) m/s	1.3 hr/ms
Case 2b	5×10^{-7} s	(1, 1) mm	(10, 4) m/s	5.8 hr/ms
Case 3a	3.33×10^{-7} s	(0.66, 0.66) mm	(25, 10) m/s	9 hr/ms
Case 3b	3.33×10^{-7} s	(0.66, 0.66) mm	(10, 4) m/s	52.6 hr/ms

It is evident from the wall times in Table 1 that the computational time increases significantly when either physical or velocity space is refined. Here, we see an increase in computational time by a factor of approximately 5 for either change. Note that Case 1 is run on 24 processors, whereas Cases 2 and 3 are run on 40 processors due to memory requirements. It is also important to point out that, in a full plasma simulation, Δt must be much smaller than the values used here to satisfy the CFL condition for ions. Therefore, it is essential to select a grid discretization that will allow for reasonable resolution but will not lead to intractable simulation times.

Steady state results for the neutral density contours in Cases 1-3 are shown in Fig. 3. For all cases with coarse velocity space (Figs. 3a, 3c, and 3e), the neutral density profile is not well resolved at the channel centerline, particularly in the plume region. For Case 1a with a single cell at the injector location (Fig. 3a), the density at the channel centerline is over-calculated. Particles injected with zero radial velocity will remain at the centerline, since the radially-adjacent cells do not contain any neutral particles moving radially toward the centerline to alter the VDF at that location. For Cases 2a and 3a (Figs. 3c and 3e), the density at the centerline in the plume region is under-calculated. Since multiple cells are used for injection, the radial flux between the cells at the centerline is non-zero, and the resultant number of particles that leave radially outward from the centerline is slightly over-calculated.

Cases 1b, 2b, and 3b with a larger number of velocity bins are shown in Figs. 3b, 3d, and 3f, respectively. Case 1b (Fig. 3b) actually has more neutral particles on centerline than the coarse case in Fig. 3a, implying that VDF resolution is not useful for this single-cell injector case. Finer VDFs are, however, useful for Cases 2b and 3b, shown in Figs. 3d and 3f. The level of improvement is similar for the 2-cell and 3-cell injector cases. For the 2-cell case, the density at the centerline is no longer under-calculated (Fig. 3d).

To demonstrate the effects of velocity bin size, VDFs in the plume region are compared in Fig. 4 for the 3-cell injector (Case 3). For this case, additional velocity bins result in an improved neutral density profile in Fig. 3f. The VDF in Fig. 4a corresponds to the density profile in Fig. 3e, and the VDF in Fig. 4b corresponds to the density profile in Fig. 3f. It is clear the the more highly resolved VDF in Fig. 4b has a much larger velocity distribution centered at ($v_r = 0$), which corresponds with more neutral particles at that location.

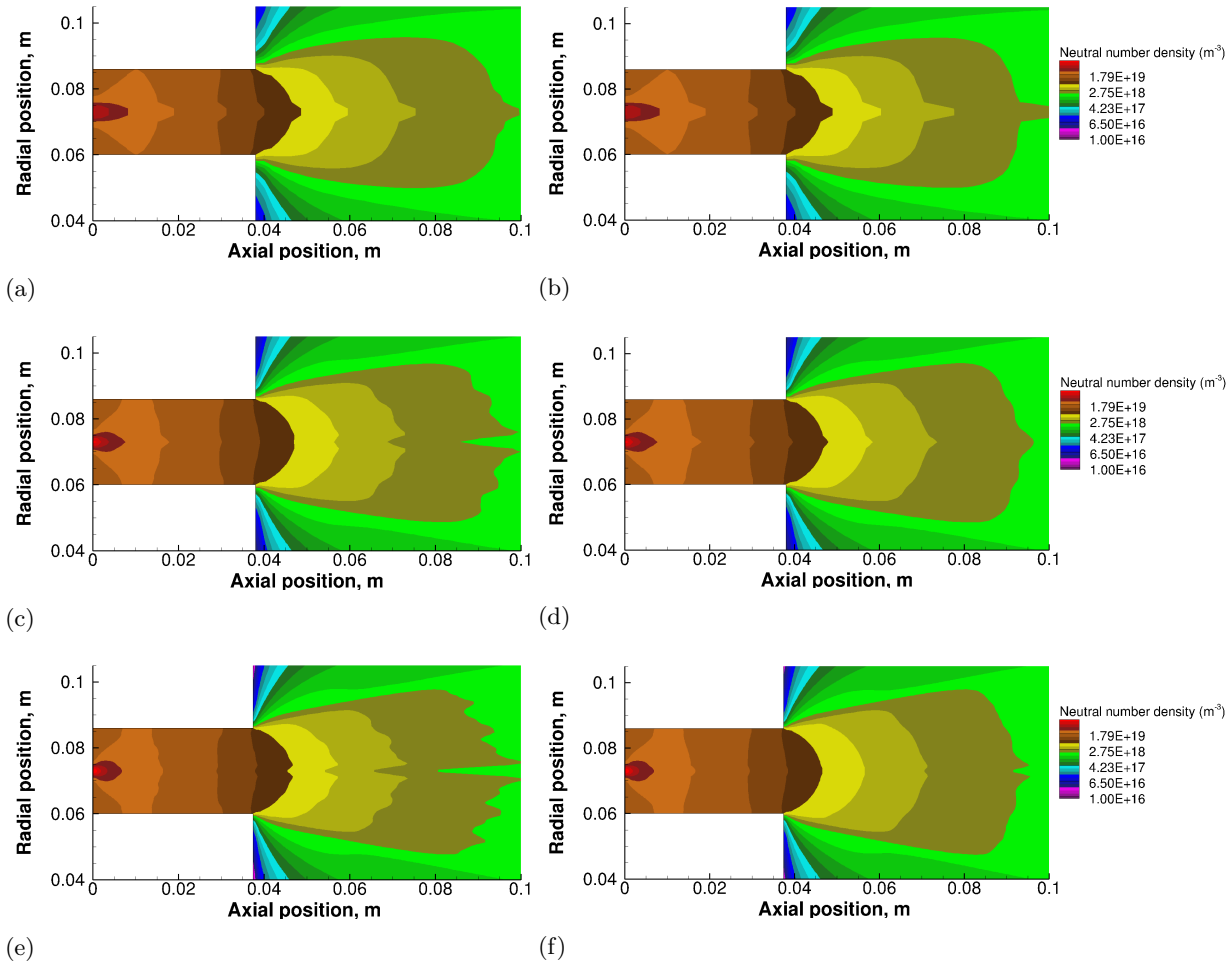

Figure 3. Steady-state neutral atom density contours for different spatial and velocity grid discretizations. (a) Case 1a, (b) Case 1b, (c) Case 2a, (d) Case 2b, (e) Case 3a, and (f) Case 3b.

Based on the results for the injection cases, it appears that it is preferable to utilize two cells for neutral atom injection in the two-dimensional DK simulation if fine velocity space discretization for neutrals is possible, since this case results in a reasonable distribution of neutral particles. To ascertain whether or not the two-cell injector is actually useful compared to a single-cell injector with the same cell size, we test another case in which we utilize the cell size and velocity discretization from Case 2b, but we assign only one cell for the inlet, located at the centerline of the channel. The results in Fig. 5 confirm that the two-cell injector in Fig. 5a better resolves the neutral atom density downstream of the injector compared to the one-cell injector in Fig. 5b, which, similarly to Case 1, over-calculates the density at the channel centerline.

B. Hybrid-DK and Hybrid-PIC simulation benchmarking, 3 kW Hall thruster

In this section, the hybrid-DK simulation is benchmarked with a comparable hybrid-PIC simulation. This effort utilizes the kinetic boundary condition update as well as the updated inlet condition and concludes a multi-part benchmarking effort, parts of which are discussed in previous work by Raisanen *et al.*[7,20] The hybrid-PIC simulation was originally developed by Koo *et al.* and is described in detail in Refs. 5 and 12, and the HET under study is the UM/AFRL P5 Hall thruster. The electron algorithm described in Section II B is identical for the hybrid-PIC and hybrid-DK simulations. Note that we do not use the alternate current calculation method described in Section III D.

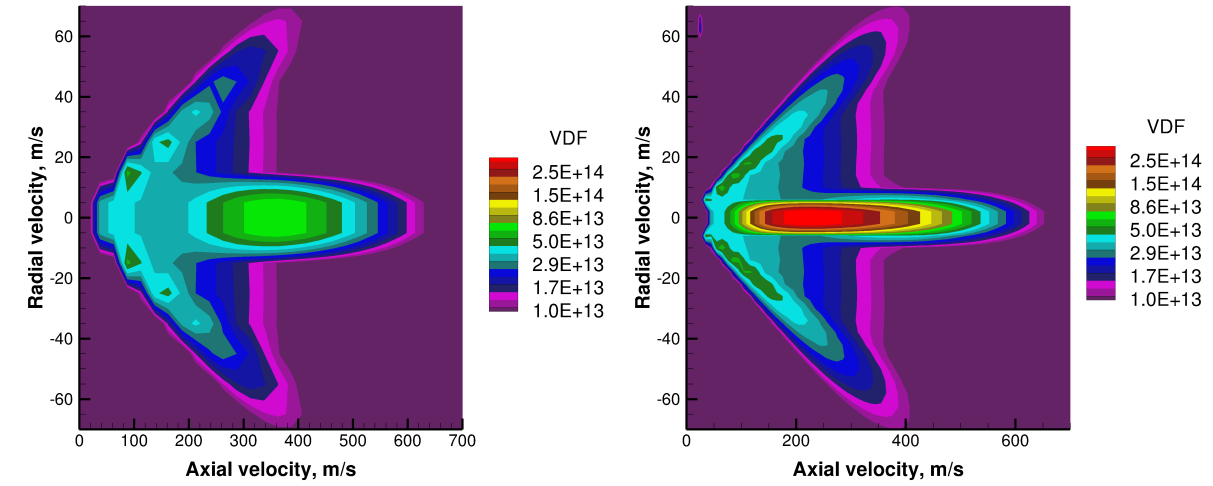

(a) (b)

Figure 4. Zoomed-in VDFs (arbitrary units) for the middle cell of the three-cell injector ($\Delta z = \Delta r = 0.66$ mm) near the right hand side of the domain at $z = 0.96$ m. Shown are (a) $\Delta v_z = 25$ m/s, $\Delta v_r = 10$ m/s and (b) $\Delta v_z = 10$ m/s, $\Delta v_r = 4$ m/s.

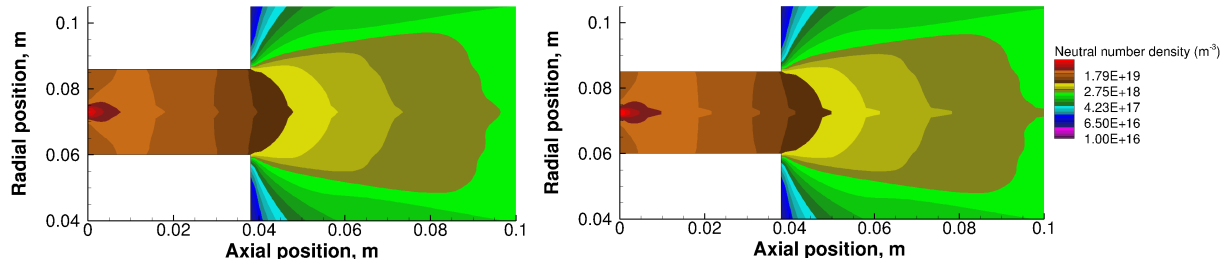

(a) (b)

Figure 5. Neutral density contour comparisons for (a) a two-cell injector versus (b) a one-cell injector with identical physical and velocity grid discretizations.

1. Hybrid-PIC simulation

In the PIC simulation, singly charged ions and neutral atoms are modeled using a technique that simulates the motion of macroparticles via a second order, classical leapfrog scheme. Neutral atoms are depleted due to ground state ionization, and collisions are accounted for using a Monte Carlo Collision (MCC) model. The MCC algorithm calculates the probability of an electron-neutral collision from the ground state based on the local plasma density, electron energy, and time step. If a collision occurs, the neutral macroparticle is changed into a singly charged ion macroparticle with the same physical properties as the parent neutral macroparticle. In practice, the number of ion macroparticles generated is too low for acceptable particle statistics, so a collision multiplier technique is applied to the MCC algorithm. The simulation results discussed in this work use a collision multiplier, $\gamma = 4$, which lies in the recommended range $2 \leq \gamma \leq 16$.[20] This value yields numerical results that are comparable with the DK simulation, in which collisional events are treated deterministically at every time step.

Particles are introduced at the inlet location according to a half Maxwellian distribution biased with axial velocity. The most probable speed, $c_{mp} = \sqrt{\frac{2kT}{m}}$, is calculated based on the anode reservoir temperature, and the effusion subroutine ensures that particles are injected according to the method described by Birdsall and Langdon, in which the normal velocity component is in the axial direction (v_z), and the two tangential

velocity components are used to calculate v_r.[21] Particles are injected at $z = 0$, randomly distributed at r locations within the confines of the anode height. Three macroparticles are injected at each time step, and the weight of each particle, W_p, is determined based on the incoming mass flow rate:

$$W_p = \frac{\dot{m}\Delta t}{m_i N_{p,injected}}. \tag{34}$$

where $N_{p,injected}$ is the number of injected particles. Note that the number density in each cell is calculated as follows:

$$n = \frac{N_p W_p}{V}, \tag{35}$$

where V is the cell volume, $V = A\Delta z$.

2. Simulation parameters

Simulation parameters are displayed in Table 2. For both the DK and PIC simulations, neutral particles fill up the domain via the anode injector prior to plasma generation. To obtain reasonable resolution with the PIC simulation using the same time step as the DK simulation, it is necessary to utilize a relatively large number of macroparticles. In the PIC simulation, a total target number of 4×10^5 ions is set, and the total neutral particle count cannot exceed 1.5×10^6. The parameters for DK velocity space are shown in Table 3.

Table 2. Hybrid-DK and PIC Simulation Parameters

Parameter	Value
Channel length, mm	38
Channel diameter, mm	26
Axial domain length, mm	100
Radial (plume) domain height, mm	146
Cell size (physical space), mm	2.0 x 2.0
Number of cells	2515
Number of λ-lines	21
Global time step, s	1.0×10^{-8}
Electron time step, s	5.0×10^{-11}
Minimum plasma density, m^{-3}	5.0×10^{12}
Minimum neutral density, m^{-3}	5.0×10^{15}
Anode potential, V	275
Anode mass flow rate, mg/s	10.2
Anode λ-line location	$z \approx 1.3$ cm
Cathode λ-line location	$z \approx 8.6$ cm

Table 3. DK velocity space parameters

Species	Dimension	Velocity range	Δv
Neutral atoms	Axial, z	$(-1.2, 1.5)$ km/s	25 m/s
	Radial, r	$(-1.2, 1.2)$ km/s	10 m/s
Ions	Axial, z	$(-16, 30)$ km/s	200 m/s
	Radial, r	$(-14, 14)$ km/s	200 m/s

In both the DK and PIC simulations, the anode reservoir and channel walls are assumed to be at a temperature of 750 K. At the anode side of the thruster, incoming neutral atoms are emitted through a slit opening with a height of 2.0 mm that is centered at ($z = 0$ m, $r = 0.073$ m). Note that for the benchmarking effort, a single cell is used the inlet in both cases, and the discretization matches Case 1a in Section IV A. The inlet neutral flow is assumed to be in the free molecular regime, as the Knudsen number is greater than

7 for a neutral density of 10^{20} m^{-3}. Note that, for the DK and PIC simulations, wall collisions are not allowed at the inlet opening. If back-streaming particles travel into the inlet, they leave the simulation domain.

The potential is fixed at the virtual anode and cathode and assumed to be constant upstream of the anode and downstream of the cathode. The electron temperature is fixed to a constant value of 0.67 eV ($\epsilon = 1.0$ eV) at the cathode, and a Neumann boundary condition is applied at the anode. Upstream of the anode and downstream of the cathode, the electron temperature decays linearly to maintain a smooth solution, and it is fixed to 1.33 eV at $z = 0$. A low electron temperature at the anode face ($z = 0$) ensures that ionization will not occur in the vicinity of the injector. Additionally, the maximum electron temperature at the anode λ-line is limited to 10.0 eV, which is necessary so that neither simulation will diverge to high, non-physical electron temperatures. Ionization is allowed everywhere, whereas in Koo's original hybrid-PIC simulation, there is no ionization upstream of the anode λ-line.[12] Both electron-wall collisions ($\alpha_w = 0.4$) and Bohm mobility ($\alpha_b = 0.006$) are considered throughout the domain. Since α_b is fixed to a constant value, the Bohm mobility acts to increase the overall electron current everywhere.

The DK simulation requires computational memory per cell on the order of $N_{v,z}N_{v,r}$ compared to $4N_p$ for the PIC simulation, where N_v is the number of grid points in velocity space and N_p is the average number of particles per cell.[9] Because it is computationally intensive, the DK simulation is parallelized using Message-Passing Interface (MPI). The domain is split into four spatial regions including the channel, the plume adjacent to the channel, the upper plume, and the lower plume, as shown in Fig. 1a. Each region utilizes an identical number of processors, and information is exchanged between adjacent processors. The simulation results discussed in this work are computed using a total of 24 processors, and the wall time is approximately 3.4 days per 1 ms of computational time. The serial PIC simulation takes approximately 14 hours to complete 1 ms of simulation time.

3. Benchmarking results

To determine the level of agreement between the DK and PIC simulations, we build cases with both high and low frequency oscillatory responses by varying some of the input parameters. We focus primarily on results for the high frequency case, which exhibits a frequency response around 100 kHz, since this case demonstrates clear improvement in the agreement of simulation results based on updated kinetic boundary conditions. Earlier results for a similar case that do not include the improved boundaries are found in Ref. 7. Although this case does not necessarily emulate the behavior of a typical HET, it benchmarks the hybrid-DK simulation with a hybrid-PIC simulation and highlights the clarity of the output in the DK results compared to the PIC results. The domain is large and the Bohm mobility coefficient is constant, so the potential fall is gradual and spreads across most of the domain. The electron temperature is fixed at the anode face and changes gradually with the potential drop, and an anode sheath is not considered, so there is no impetus for periodic ionization bursts and neutral replenishment which accompany a low-frequency mode.

The discharge current profiles in Fig. 6a exhibit nearly the same mean value (DK: 8.6 A, PIC: 8.8 A), compared to a previous study where the mean value of the current varied by approximately 1 A.[7] The PIC response in Fig. 6b shows some deviation in the current amplitude, while coherent oscillations are clearly seen in the DK response. Both data sets show a high frequency oscillation near 100 kHz. The PIC results are noisy, but the DK results exhibit distinct frequencies at 97 kHz and 194 kHz. This high frequency behavior might be described by the ion transit time-oscillation, which typically has a frequency in the 100-500 kHz range and a period on the order of the transit time of ions passing through the acceleration region. It is associated with an oscillating electric field and the formation of a tail in the ion energy distribution function.[22] However, an oscillation of this frequency could also occur due to the coupling of the electron pressure term in the drift-diffusion approximation for the electron flux, therefore making it numerical in nature.[23] Time-averaged hybrid-DK and hybrid-PIC plasma properties are shown in Figs. 6c and 6d. A sampling interval of 1 μs is used for data collection. The PIC neutral and ion density profiles at the thruster channel centerline in Fig. 6c show reasonable agreement with the corresponding DK properties, and based on the agreement in the density gradient near the anode, it is clear that the injection schemes at the left hand side of the domain are the same. The average electron temperature and potential profiles for the two simulations in Fig. 6d also exhibit similar trends.

While the aforementioned benchmarking case highlights distortions in the PIC discharge current response due to statistical noise, it does not capture low frequency transient plasma physics. HETs typically exhibit repetitive, low frequency oscillations known as *breathing mode* oscillations, so it is worthwhile to include results that exhibit this type of response. To elicit a low-frequency mode with the hybrid-DK and PIC

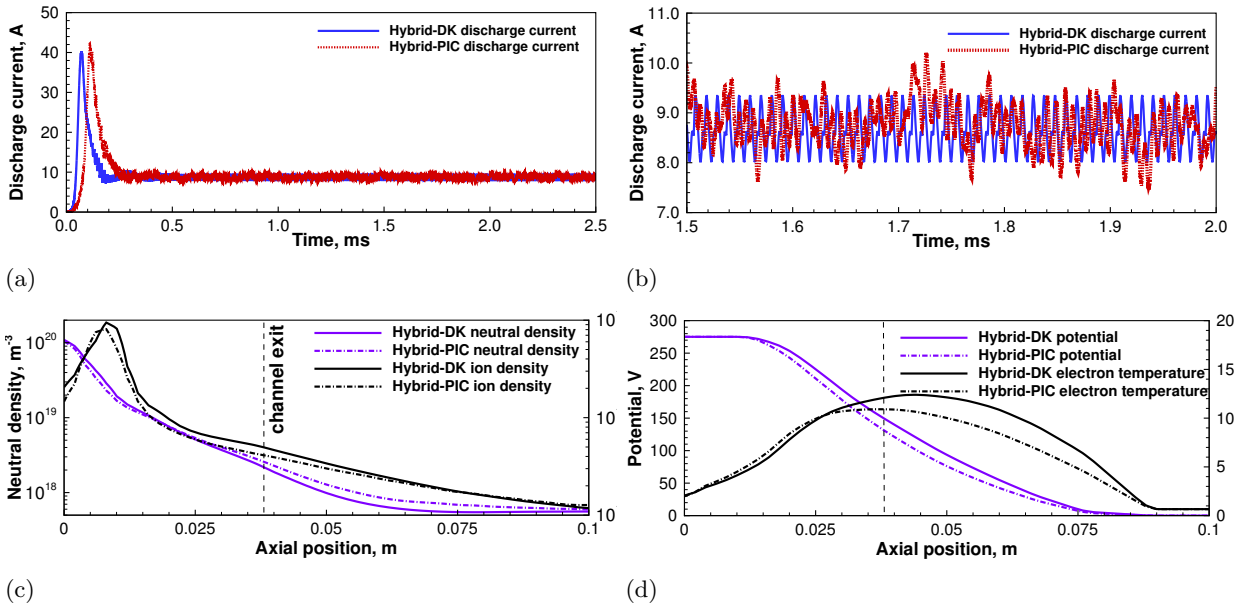

Figure 6. Hybrid-DK and hybrid-PIC benchmarking results for a high frequency case. In (a), the full discharge current profile is shown, and in (b), several oscillations are highlighted. The time-averaged plasma and neutral densities along the thruster channel centerline are shown in (c), and the time-averaged plasma potential profile and electron temperature are shown in (d).

simulations, it is necessary to alter some of the input parameters. We neglect Bohm transport altogether and consider only electron-wall collisions. To ensure that the potential drop does not spread too far downstream, the virtual cathode is shifted closer to the channel exit ($z \approx 5.0$ cm). We consider a simple, one-dimensional anode sheath model (Eq. (33)) in the cells adjacent to the anode wall ($z = 0$), and we also assume that the Boltzmann relation applies for the calculation of the electron density inside the sheath. Sufficient oscillatory behavior is achieved when the electron temperature upstream of the anode λ-line corresponds to the relationship in Eq. (36):

$$T_e(\lambda) = T_e(\lambda_a) \exp(-0.1(\lambda_a - \lambda)). \tag{36}$$

This relationship ensures that the temperature will decay slightly upstream of the anode λ-line and promotes variation in the electron temperature over time and in space, promoting cyclical ionization, sufficient for benchmarking. It is possible that the anode sheath is important to limit the electron current. If the sheath model is not applied, we observe that the hybrid-PIC simulation becomes devoid of neutral macroparticles inside the channel at certain instances in time, rendering the PIC solution non-physical.

Lastly, the electron-wall collision frequency is lowered from $\alpha_w = 0.4$ to $\alpha_w = 0.2$, and this promotes greater variation in the discharge current amplitude, indicating that the balance between the electron collision frequency and inelastic energy losses is important. In Fig. 7, three current oscillations are highlighted. The time instances are shifted between the hybrid-PIC and hybrid-DK results so that the dynamic oscillations of the two results are comparable. A Fourier analysis of the total data reveals a low frequency of 6.4 kHz in the DK case, whereas the PIC data exhibits a low frequency oscillation around 7.0 kHz. The mean DK current for the data set is 6.3 A, while the PIC current is slightly higher at 6.8 A. There is no significant difference between the DK and PIC ion and electron current contributions. Although not shown, plasma properties exhibit similar values and trends for the low frequency case. However, additional work is required to ensure that the plasma response at the anode sheath location is sufficiently resolved.

V. Conclusion

In this study, boundary conditions were modified for a two-dimensional hybrid-DK simulation. Diffuse wall boundary conditions ensure particle conservation and resulted in improved agreement between the

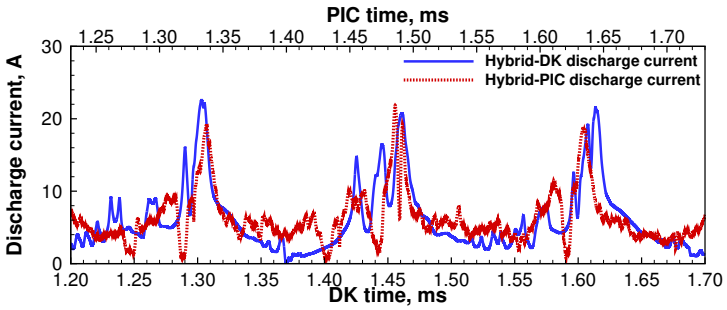

Figure 7. Discharge current vs time for 10 kHz frequency response.

plasma response for the hybrid-DK model and a comparable hybrid-PIC model. The DK inlet boundary condition was examined with respect to grid discretization, and convergence was found for reasonable resolution of the neutral distribution downstream of the inlet location. Improvements were made to the electron model, i.e. the current solver was modified to ensure that the anode sheath potential is taken account. In future, updates including a wall plasma sheath model are required so that the hybrid-DK model is better equipped to resolve complex physical processes inside the thruster channel.

Acknowledgments

The authors gratefully acknowledge financial support provided by the Air Force Office of Scientific Research, Grant No. FA95550-17-1-0035. The first author would like to acknowledge Dr. Ken Hara and Alexander Vazsonyi for useful discussions over the course of this work.

References

[1]Morozov, A. I., "The Conceptual Development of Stationary Plasma Thrusters," *Plasma Physics Reports*, Vol. 29, No. 3, 2003, pp. 235-250.

[2]Boeuf, J. P. and Garrigues, L., "E × B electron drift instability in Hall thrusters: Particle-in-Cell simulations vs. theory," *Physics of Plasmas*, Vol. 25, No. 061204, 2018.

[3]Fife, J. M., "Hybrid-PIC Modeling and Electrostatic Probe of Hall Thrusters," Ph.D. Dissertation, Aeronautics and Astronautics Dept., Massachusetts Institute of Technology, Cambridge, MA, 1998.

[4]Hagelaar, G. J. M., Bareilles, G., Garrigues, L., and Boeuf, J. P., "Two dimensional model of a stationary plasma thruster," *Journal of Applied Physics*, Vol. 91, No. 5592, 2002.

[5]Koo, J. W. and Boyd, I. D., "Modeling of anomalous electron mobility in Hall thrusters," *Physics of Plasmas*, Vol. 13, No. 033501, 2006.

[6]Batishchev, O. V., "Semi-Analytical Adaptive Vlasov-Fokker-Planck-Boltzmann Methods," in *Eulerian Codes for the Numerical Solution of the Kinetic Equations of Plasmas*, edited by M. Shoucri, Nova Science Publishers Inc., New York, 2010, Chap. 7.

[7]Raisanen, A. L., Hara, K., and Boyd, I. D., "Two-dimensional Hybrid-Direct Kinetic Simulation of a Hall Thruster," *AIAA Propulsion and Energy Forum*, AIAA-2018-4809, 2018.

[8]Hara, K., Boyd, I. D., and Kolobov, V. I., "One-dimensional hybrid-direct kinetic simulation of the discharge plasma in a Hall thruster," *Physics of Plasmas*, Vol. 19, No. 113508, 2012.

[9]Hara, K., "Development of Grid-Based Direct Kinetic Method and Hybrid Kinetic Continuum Modeling of Hall Thruster Discharge Plasmas," Ph.D. Dissertation, Dept. of Aerospace Engineering, University of Michigan, Ann Arbor, MI, 2015.

[10]Arora, M. and Roe, P. L., "A Well-Behaved TVD Limiter for High-Resolution Calculations of Unsteady Flow," *Journal of Computational Physics*, Vol. 132, No. CP965514, 1997.

[11]Hara, K., "An overview of discharge plasma modeling for Hall effect thrusters," *Plasma Sources Science and Technology*, Vol. 28, No. 044001, 2019.

[12]Koo, J.W., "Hybrid-PIC MCC Computational Modeling of Hall Thrusters," Ph.D. Dissertation, Dept. of Aerospace Engineering, University of Michigan, Ann Arbor, MI, 2005.

[13]Boeuf, J. P. and Garrigues, L., "Low frequency oscillations in a stationary plasma thruster," *Journal of Applied Physics*, Vol. 84, No. 7, 1998.

[14]Puech, V. and Mizzi, S., "Collision Cross Section and Transport Parameters in Neon and Xenon," *Journal of Physics D: Applied Physics*, Vol. 23, 1991, pp. 1974-1985.

[15]Vincenti, W. G. and Kruger, C. H., *Introduction to physical gas dynamics*, Wiley, New York, 1965.

[16]Boyd, I. D. and Schwartzentruber, T. E., *Nonequilibrium Gas Dynamics and Molecular Simulation*, Cambridge University Press, Cambridge, UK, 2017, pp. 29-44.

[17]Ahedo, E., Martinez-Cerezo, P.,and Martinez-Sanchez, M., "One-dimensional model of the plasma flow in a Hall thruster," *Physics of Plasmas*, Vol. 8, No. 3058, 2001.

[18]Parra, F. I., Ahedo, E., Fife, J. M., and Martinez-Sanchez, M., "A two-dimensional hybrid model of the Hall thruster discharge," *Journal of Applied Physics*,Vol. 100, No. 023304, 2006.

[19]Hara, K. and Hanquist, K., "Test Cases for Grid-Based Direct Kinetic Modeling of Plasma Flows," *Plasma Sources Sci. Technol.*, Vol. 27, No. 065004, 2018.

[20]Raisanen, A. L., Hara, K., and Boyd, I. D., "Assessment of a two-dimensional hybrid-Direct kinetic Simulation of a Hall thruster," *AIAA Propulsion and Energy Forum*, AIAA-2017-4727, 2017.

[21]Birdsall, C. L. and Langdon, A. B., *Plasma Physics via Computer Simulation*, IOP Publishing, Bristol, England, UK, 1991. pp. 387-416.

[22]Lim, Y., Choe, W., Mazouffre, S., Park, J. S., Kim, H., Seon, J., and Garrigues, L., "Nonlinear ion dynamics in a Hall thruster plasma source by ion transit-time instability," *Plasma Sources Science and Technology*, Vol. 26, No. 3, 2017.

[23]Hara, K., "Non-oscillatory quasineutral fluid model of cross-field discharge plasmas," *Physics of Plasmas*, Vol. 25, No. 123508, 2018.

[24]Reid, B. M., "The influence of neutral flow rate on the operation of Hall thrusters", Ph.D. Dissertation, Dept. of Aerospace Engineering, University of Michigan, Ann Arbor, MI, 2009.

[25]Hofer, R. R., Katz, I., Mikellides, I. G., Goebel, D. M., Jameson, K. K., Sullivan, R. M., and Johnson, L. K., "Efficacy of Electron Mobility Models in Hybrid-PIC Hall Thruster Simulations," *AIAA Joint Propulsion Conference*, AIAA-2008-4924.